Int. J. Electrochem. Sci., 16 **(2021)** Article ID: 210839, doi: 10.20964/2021.08.39

International Journal of ELECTROCHEMICAL SCIENCE
www.electrochemsci.org

Solidification Process, Mechanical and Electrochemical Properties of Amorphous and Nanocrystalline Iron Alloy for a Power System Application

Xiaozhong Xu[*], *Jiangang Li, Jiajie Yu, Xiaoqin Jiang, Gan Shao*

Sategrid Ningbo Electric Power Supply Company, Ningbo 315000, China
[*]E-mail: Xu-Xiaozhong@protonmail.com

Received: 26 March 2021/ *Accepted:* 15 May 2021 / *Published:* 30 June 2021

Nanocrystalline alloy is widely used in power systems because of its advantages of high magnetic conductivity, low loss, high strength and high resistivity. The amorphous method was used to prepare iron with the best amorphous thin strip processing parameters: the size of circular quartz tube was 0.8 mm; the distance between the nozzle and the surface of copper roller was 0.5 mm; the linear speed of copper roller surface was 41 m/s; the pressure difference between the inside and outside of quartz tube was 0.03 MPa; the spray angle was 0°. The solidification of the Fe based nanocrystalline alloy was studied by the solidification morphology, X-ray diffraction analysis, magnetic properties and mechanical properties. According to EIS studies, a 360K undercooling temperature leads to an increase in the penetration of electrolyte ions into electrode structures due to the formation of a high surface area and a high electron-transfer rate. The experimental results show that the undercooling of the alloy melt can be significantly improved by the amorphous method; the crystallization process of the prepared nanocrystalline alloy was controlled by the growth of the nanocrystalline; the prepared Fe based nanocrystalline alloy was more suitable for the common mode choke core, and can reflect different degrees of magnetic properties under the influence of different annealing temperatures; the prepared Fe based nanocrystalline alloy was better than the coarse-grained alloy. It had higher microhardness and elastic modulus. The solidification sensitivity of this nanocrystalline alloy was completely confirmed by these experimental findings.

Keywords: Nanocrystalline iron Alloy; Solidification process; Mechanical property; Electrochemical property; Power system

1. INTRODUCTION

In the outline of "solving the global greenhouse effect," the World Conservation Fund pointed out that "amorphous and nanocrystalline materials are promising new materials for energy conservation." Nanocrystalline alloy is a new type of soft magnetic alloy, which has been developed for more than 10 years. Its application has been extended from small electronic equipment to large-

scale high-voltage power systems. The application of soft magnetic materials can almost cover every power equipment in the power system, some of which are used as supporting products, some of which are directly used [1]. For example, power transformer, reactor, mutual inductor, etc. in the transmission and distribution system, as well as mutual inductor for high-voltage circuit breakers, mutual inductor for fully enclosed combined electrical appliance, etc. All of the above are equipment with winding and iron core, which will be applied to soft magnetic materials more or less.

Nanocrystalline alloy is developed on the basis of amorphous alloy [2], that is to say, after heat treatment at 500-600ºC, the amorphous alloy with a grain size of only 10-20 nm is formed, so that it has excellent performance. In addition to the high magnetic conductivity, low loss, wear resistance, corrosion resistance, high strength, high resistivity, good toughness and electromechanical coupling possessed by the amorphous alloy [3, 4]. In addition to the characteristics of large combining coefficient, it also has the unique performance of extremely high permeability under the weak field (0.08 A/m), which is opposite to the reduction of the magnetism of conventional soft magnetic alloy with the decrease in grain size. Therefore, the use of nanocrystalline alloy can further reduce the loss [5], especially if the high-frequency loss is very low. The magnetization curve can be obtained through the heat treatment process according to the demand. The hysteresis loop can be round or flat or rectangular, so it can be a nano crystal alloy that is widely used in many fields.

Since 2000, China's electric power industry has started the revolution of product and material manufacturers. A large number of traditional mechanical energy meters have been replaced with digital energy meters with high accuracy and small loss. Anti-theft and electric shock security devices have been widely used [6]. There are also many scientific and technological achievements in aerospace, lunar exploration, satellite, etc., which are inseparable from a new type of magnetic material applied to electromagnetic and inductive components. Material nanocrystalline alloy material [7]. The soft magnetic properties of nanocrystalline alloys have the advantages of all kinds of traditional soft magnetic materials, such as high saturation magnetic induction strength, high permeability and low loss, etc., which meet the needs of various electronic equipment to develop to high efficiency, energy saving, miniaturization and integration, and the cost is low. Therefore, this paper focuses on the solidification sensitivity of Fe based nanocrystalline alloys which are often used in power systems. Fe based nanocrystalline alloy materials have both high saturation magnetization of Fe based amorphous alloy and high permeability, low loss of Co based amorphous alloy, and low cost [8]. Therefore, they can replace Co based amorphous alloy, fine permalloy and ferrite, and are widely used in the field of high-frequency power electronics and electronic information, with the purpose of reducing volume and cost. In a power system, all materials are required to have high precision and low loss. Therefore, nanocrystalline alloy is also very suitable for applications with high requirements for weak field permeability and low requirements for high frequency loss [9, 10]. It is of great significance to apply nanocrystalline alloy as a high-tech material to the power system so that it can give full play to its excellent soft magnetic properties. Nanocrystalline alloy is mainly used in the following equipment in power systems: measuring current transformer, measuring current transformer for fully enclosed combined electrical appliances, etc [11].

At present, a large number of scholars in China and abroad have studied the properties of nanocrystalline alloy materials. In order to obtain high-quality nanocrystalline alloy materials, it is

necessary to heat treat the amorphous alloy materials [12]. In 1988, Luco et al. developed the isothermal annealing method through many experiments and summaries, which is simple in process, low in cost and widely used quickly. This method requires the amorphous alloy to be heat treated in an inert atmosphere. The sample is heated to a predetermined temperature at a rapid rate, and then cooled with the furnace after a period of time at that temperature. The main parameters of this method are: heating rate, holding temperature, holding time. This method can produce nanocrystalline alloy particles with sizes ranging from 10 to 20 nm. In 1993, Noh et al. used the distributed annealing method to heat treat the amorphous alloy, and obtained better soft magnetic properties. The distributed annealing method is an improvement of the equal temperature annealing method. The method is to carry out the low temperature preheating treatment for a period of time before the isothermal annealing treatment. In order to improve the nucleation rate, then carry out the crystallization temperature. The process of heat treatment makes the grains of ferromagnetic phase grow [13].

When the amorphous alloy is annealed, a directional magnetic field is added. This method is called the magnetic field annealing method. The purpose is to make the alloy after heat treatment have uniaxial magnetocrystalline anisotropy [14]. In 1989, Yoshizawa annealed Finemet series products in a longitudinal and transverse magnetic field to study the effect on the properties of amorphous alloy. K. Suzuki et al. further annealed them in rotating magnetic field. The results showed that the coercivity of amorphous nanocrystalline alloy annealed in this way decreased. The results show that the magnetic field annealed amorphous alloy produces uniaxial induced anisotropy. In addition, Herzer proposed in his theory that the average process of magnetocrystalline anisotropy in amorphous nanocrystalline soft magnetic alloy can change Ku.

In order to effectively study the properties of Fe based nanocrystalline alloys which are often used in power systems, the amorphous method is selected to prepare Fe based nanocrystalline alloys, and the solidification sensitivity of the nanocrystalline alloys is studied through the aspects of solidification structure appearance, magnetic properties and mechanical properties.

2. MATERIALS AND METHODS

2.1. Preparation Process

There are many preparation methods of nanocrystalline alloy. In this paper, the amorphous method with the characteristics of simple process and low cost was selected. The amorphous method is widely used in the industrial production process. The amorphous method needs to first prepare the amorphous alloy strip with the required cost through relevant methods, and then make the sample crystallized to the optimal state through appropriate heat preservation annealing process to obtain high-quality comprehensive soft magnetic properties [15].

The preparation process of nanocrystalline alloy by amorphous method was as follows. First, the master alloy was put in the quartz tube, and then heated through the induction coil around the quartz tube. The rapid heating rate was used to raise the temperature to more than 1300ºC in a short time. Following the presentation of the master alloy in the molten state, the master alloy in the flowing

state sprayed the molten alloy to the high-speed rotating pass with constant pressure. The molten alloy rapidly cooled and was thrown out [16], on the copper roller with cooling water, resulting in a continuous amorphous strip. The cold speed of forming amorphous thin strip was generally 106 k/s. In order to obtain a higher cold speed, the copper roller needs to rotate at a very fast speed. Using this method, the thickness of the strip thrown out was limited, generally not more than 50 μM. This preparation process was quite different from the traditional hot pressing and cold rolling.

2.2. Alloying Element

After scraping the oxide skin on the surface of the alloy raw materials with ultrasonic washing, the ingredients were weighed using an electronic balance with a precision of 0.002 g according to the planned nominal composition [17]. Table 1 shows the alloy elements used to make the Fe based nanocrystalline alloy, as well as their purity.

Table 1. Alloying elements used in the preparation of alloys and their purity.

Alloy element	purity/%
Fe (3-5 mm)	99.98
Fe (20 mm)	99.92
Si	99.98
Cu	99.96
Y	99.89
Nb	99.98
B	99.89
V	99.98

2.3. Sample Preparation

2.3.1. Preparation of Master Alloy

The narrow-band master alloy ingot was created in this study by melting it in a non-consumable electric arc furnace with high-purity argon as a shield [18]. The non-self-consuming electric arc furnace zhw-600a was used to prepare the master alloy, and the physical image of the non-self-consuming electric arc furnace is shown in Figure 1.

Figure 1. Non-consumable electric arc furnace physical map.

Each ingot was about 35-45 g. The weighed sample material was placed in the electric arc furnace's copper crucible. The chamber was vacuumed to about 0.001 Pa, filled with high-purity argon, first molten the zirconium block in the center of the dry pot, fully purified the chamber, and then melted the sample; the smelting current was about 320 A. The sample was smelted 4 times repeatedly to ensure that the raw materials in the sample are fully mixed evenly and reach chemical uniformity. Weigh the melted sample again to ensure that the difference between the mass and that at the time of batching is less than 1%.

In this paper, the master alloy used to prepare Fe based nanocrystalline alloy was prepared by a self-developed vacuum induction melting furnace. The heater of smelting system was made of copper tube wound induction coil [19], which was connected with the medium frequency power supply by a water-cooled cable. The metal liquid was poured by manual tilting. The smelting system was equipped with thermocouples as temperature feedback signals for temperature control. The temperature feedback signals were provided to the temperature controller to control the output power. The smelting power was 20 kW, and the weight of a single furnace smelting ferroalloy was about 2.5 kg. In the smelting process, the alloy was evenly mixed by repeatedly shaking the tilt casting rod, smelting and holding for 20 minutes and smelting twice, so as to ensure that the raw materials in the sample were fully mixed evenly [20], achieving chemical uniformity. The melted sample was weighed again to ensure that the difference between the mass and that at the time of batching was less than 6%.

2.3.2. Principle of Preparing Single Roll Belt Rejection

The experimental preparation of Fe based nanocrystalline alloy belt slinger adopts the original imported induction melt fast quenching belt slinger from Japan. The vacuum degree of the furnace body was first pumped to below 0.005 Pa after the sample was placed, and the shielding gas was high-purity argon. The metal sample is inductively melted through the induction coil around the quartz tube until the sample shows a melting state (the general temperature can reach 1300 photos for a short period of time, in order to make the sample fully melt [21], so as to ensure that the sample presents a fluid state. At the end of preparation, a constant argon pressure (0.003 MPa, a constant pressure gas

storage tank was added outside the furnace chamber) was used to spray the alloy in the form of fluid onto a high-speed rotating copper roller, and the inner part of the copper roller was also provided with cooling water to ensure the determination of the cooling speed, so as to rapidly cool the material for preparing the belt. The following is a sample of amorphous thin strip tossed away by single roll belt denial, as seen in Figure 2.

Figure 2. Thin strip sample taken out from a single roll.

2.3.3. Preparation Parameters of Amorphous Ribbons

Because, for the manufacture of amorphous ribbons, the quartz nozzle should not be too large [22], with too big a nozzle would cause the molten metal solution to "self-flow" under the influence of self-weight, resulting in mistakes in the experiment and inability to effectively generate the needed amorphous ribbons. As a result, a round quartz tube with a diameter of roughly 0.8mm was used for this study.

The distance between the nozzle and the copper roller's surface has a significant impact on the strip's width and thickness. The spraying distance should be lowered as much as feasible to ensure the precision and dependability of the testing results. The distance between the nozzle and the copper roller surface in this research was 0.5mm.

Because the high-speed rotating copper roller will produce a reverse shear force [23] on the strip thrown out, in addition, the cooling rate of the amorphous strip is uneven, and the amorphous strip will generate internal pressure due to the influence of temperature gradient. This internal stress can be eliminated by rapid vacuum heat treatment below temperature. In this paper, the surface linear velocity of the copper roller was set as 41m/s.

The expression of pressure difference inside and outside the quartz tube is shown in formula (1).

$$\Delta P = P_0 - P_l \qquad (1)$$

where P_0 represents the external pressure of a quartz tube; P_l represents the pressure of argon rushing into the wall. The flow rate of molten metal liquid through the quartz tube orifice is determined by the diameter of the nozzle and the jet pressure. When the speed of the copper roller is

fixed and the size of the quartz tube nozzle is fixed, the amorphous strip thickens with the increase of the pressure difference. In this paper, the experimental setting of the internal and external pressure difference of the quartz tube was 0.03 Mpa.

The temperature during spraying will affect the viscosity of the alloy melt. If the temperature is too high during spraying, the melt is prone to sintering. If the temperature is low, the melt will have strong fluidity, which will lead to fracture or discontinuity of the strip. Therefore, the appropriate spraying temperature is also a very important factor [24]. In general quantitative analysis, the spray temperature is required to be higher than the melting point of the alloy by about 100K, and the melt temperature can be measured by an infrared thermometer. However, due to experimental equipment limitations, we had summarized many experiments that the melt can change color with temperature increase, generally the gradual change from red, yellow to white.

When the quartz tube with a circular nozzle is slightly inclined, the thickness of the strip will slightly increase, but the degree of influence is much smaller than other parameters. In this paper, the injection angle was chosen as 0 degree, that is, the quartz tube was suspended on the top of the copper roller, and the melt hammer fell on the surface of the copper roller.

In this work, the technological parameters for the preparation of amorphous ribbons are shown in the table below.

Table 2. Process parameters

Process parameters	Size standard
Nozzle size	0.8 mm
Copper roller speed	41 m/s
Spout to copper roller spacing	0.5 mm
Intracavity vacuum	0.0002 Pa
Pressure difference	0.03 MPa
Intracavitary atmosphere	99.999% High purity argon
Jet angle	0°

2.3.4. Preparation of Annealed Samples

After the amorphous alloy is made, it needs to be annealed at different temperatures to obtain nanocrystalline alloy, so as to improve the soft magnetic properties. The sample was vacuum sealed with quartz tube throughout the annealing process. The quartz tube was placed in the heat treatment furnace for isothermal annealing once the vacuum was less than 0.0006 Pa. The quartz tube was removed from the test after the required time had passed and rapidly immersed in water to cool to room temperature. After annealing, the surface of the sample is free of oxidation traces and still shows metallic luster. The box type annealing furnace used in the test is shown in Figure 3.

Figure 3. Vacuum annealing furnace physical map.

2.4 Electrochemical, structural and morphological characterizations

EIS measurements were performed in a standard three-electrode electrochemical cell utilizing a CHI 660D potentiostat in a frequency range of 0.1kHz to 1MHz at 5mV AC voltage utilizing a produced Fe based nanocrystalline alloy, Ag/AgCl, and Pt rod as working, reference, and counter electrodes, respectively. The crystallinity and structure of the samples were investigated using an Xpert Pro X-ray diffractometer (XRD) with a wavelength of 1.5404 (Cu Kα) at 40KV and 30mA. The morphology of the prepared sample was examined using scanning electron microscopy (SEM, Hitachi S4700, Japan).

3. RESULTS

3.1. Solidification Morphology

The Fe based nanocrystalline alloy has typical eutectic properties, and its melting point is about 1105 Kv [25]. The mixed structure of regular primary dendrite and irregular eutectic structure was achieved when the alloy melt solidified at a lower undercooling (△T=40 K). Figure 4a depicts the solidified structure. The remaining grains, with the exception of the primary dendrite, were ranged in size from 4 to 10μm.

There was no evident primary dendrite phase in the solidification structure when the alloy was undercooled to △T=100 K, as illustrated in Figure 4b. It was only composed of uneven eutectic structure at the time, with grain sizes ranging from 1 to 5μm.

The solidification structure of the alloy was dramatically different when the undercooling was raised to 200 K, as illustrated in Figure 4c The whole structure was a two-phase coexisting structure with disordered two-phase distributions that were coupled to create a network, which was compatible with Nagase's solidification structure following liquid Spinodal decomposition [26], that is, it had a

typical network structure of liquid Sipnodal decomposition. The network appears to have established at this time, as seen in Figure 4c. The structure was made up of two subnetworks, one with smaller grains and the other with bigger grains averaging 70 nm in size. Figure 4d shows that when subcooling was increased to 360 K, the grain distribution in the whole solidification structure was highly uniform and fine, with an average grain size of roughly 40 nm. The white appearance in Figure 4d still had a network structure at this point, but the black phase deteriorated had no network structure at all. It may be attributed to the network structure being very small, the latent heat of crystallization causing the network structure to fuse during solidification, or the surface tension dividing the supercooled liquid network into micro droplets, which were maintained in the subsequent solidification process [27-29].

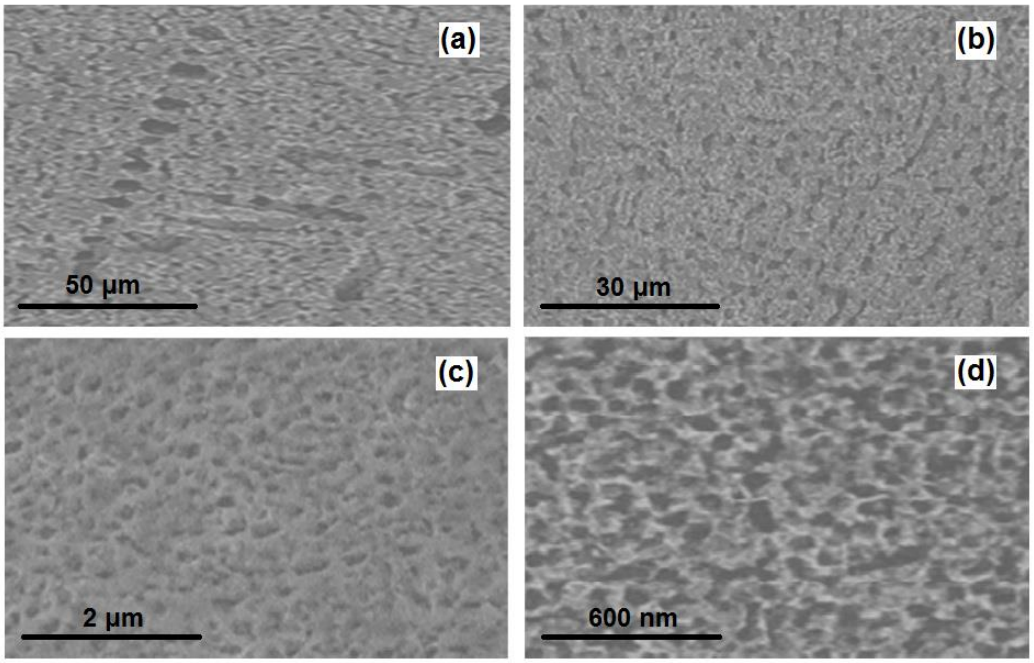

Figure 4. Solidification structure of Fe based nanocrystalline alloy under different cooling conditions (a) 40 K (b) 100 K (c) 200 K (d) 360 K.

The results indicated that the undercooling of the alloy melt can be significantly improved by the amorphous method, and the supercooling of about 0.3nTm was obtained. Under the deep undercooling condition, the solidification structure of the alloy melt had the network structure formed by the liquid Spinodal decomposition, and under the large undercooling condition, the block nanocrystalline with a small size and uniform structure can be prepared Gold material.

3.2. Electrochemical test

EIS analysis in open circuit potential (OCP) was used to further characterize the transfer of carriers and ion diffusion by applying an AC voltage of 5 mV and a frequency of 0.1kHz to 1MHz (Fig. 5). The generation of electrode and electrical impedance of contact between active materials on the electrode surface and electrolyte can be implied by the semicircle in the high frequency range associated with surface films (R_{SEI}). Furthermore, the charge transfer mechanism is similar to the

semicircle in the medium frequency range, and it can be denoted by the interfacial charge-transfer resistance (R_{ct}) [30].

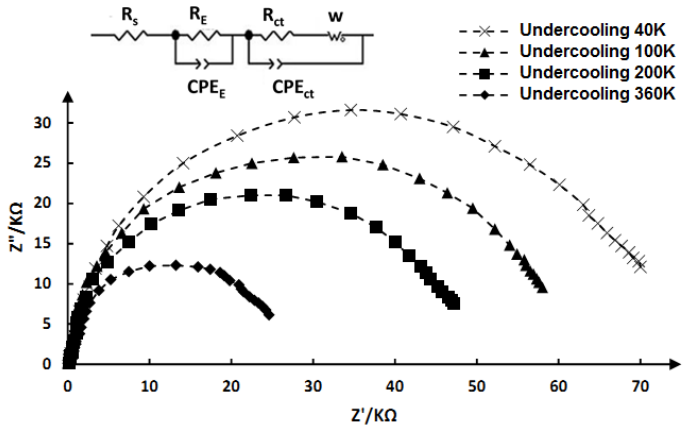

Figure 5. The EIS analysis of Fe based nanocrystalline alloy with various undercooling temperatures in OCP by applying an AC voltage at 6 mV and the frequency from 0.001Hz to 105Hz. Inset figure shows an equivalent circuit model used for EIS data fitting.

Solid state Warburg impedance (W), which assigns to the diffusion of solid state ions into the porous matrix of electrode material, is responsible for the tail in the low frequency range [30, 31]. As a consequence, Figure 5 and Table 3 show the effects of the EIS data fitting. Where RE denotes electrolyte resistance and CPE denotes a constant-phase factor that describes the depressed semicircle created by an ohmic resistor connected in parallel. As shown, the R_{SEI} and R_{ct} of the undercooling 360K sample are lower than those of the other samples, suggesting that the 360K undercooling temperature reduces the R_{SEI} and R_{ct} while increasing ion diffusion into the electrode structure. The use of a 360K undercooling temperature to modify electrodes resulted in a high electron transport rate and a large surface area, which was useful for power system applications.

Table 3. Results of EIS analysis

Undercooling temperature	R_{ct} (kΩ)	R_{SEI} (kΩ)	R_E (Ω)
40 K	73.5	49.4	72.9
100 K	61.2	32.6	83.8
200 K	49.8	24.9	73.7
360 K	27.3	14.7	76.4

3.3. X-ray Diffraction Analysis

Figure 6 shows the relationship between the microstructure parameters obtained from the X-ray diffraction results and the annealing temperature. Figure 6a shows the relationship between grain size

and annealing temperature. Typically, when grain size decreases, the X-ray diffraction peak increases broader [32]. Figures 6b and 6c show the relationship between crystallization fraction and lattice constant and annealing temperature, respectively.

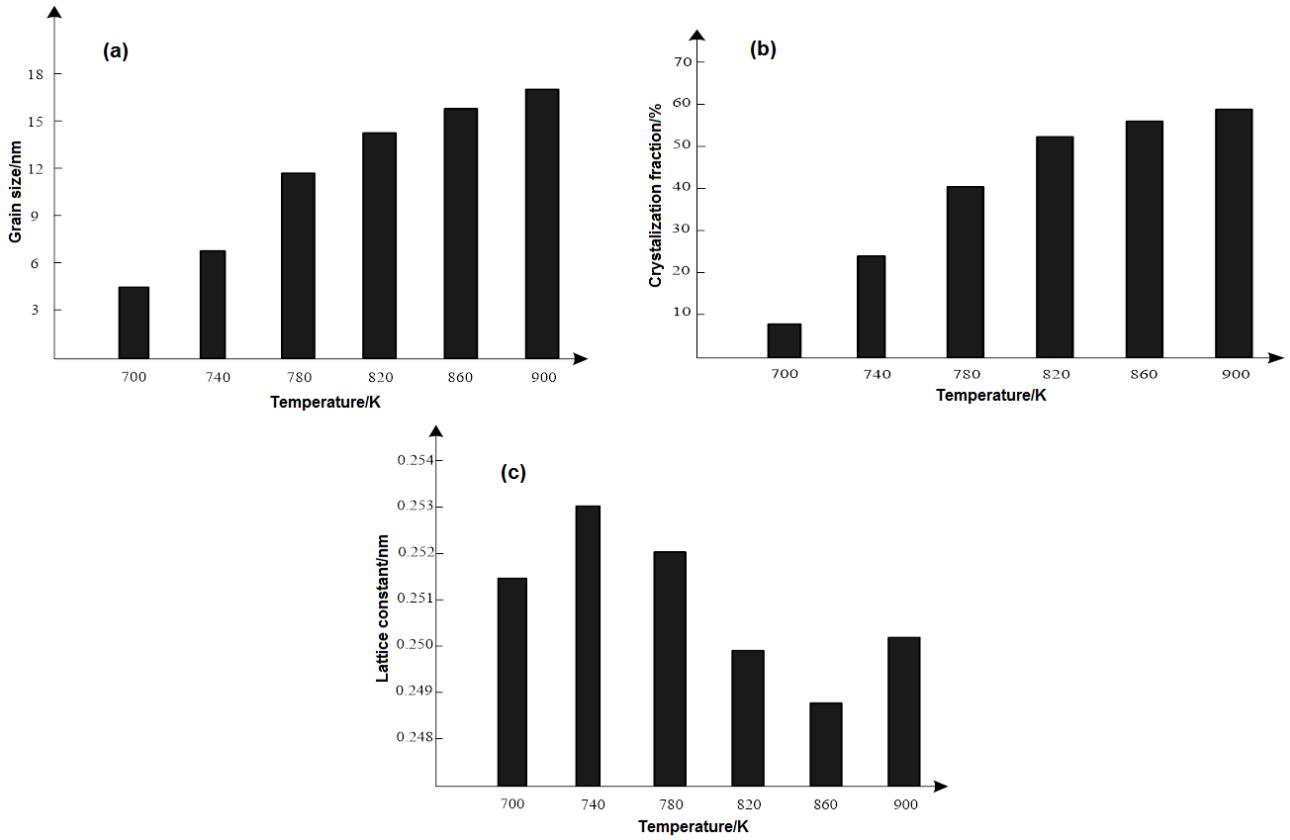

Figure 6. Microstructure parameters of Fe based nanocrystalline alloy (a) Grain size and annealing temperature, (b) Crystallization fraction and annealing temperature, (c) Lattice constant and annealing temperature

The lattice constant of the created Fe based nanocrystalline alloy was less than that of pure iron, as shown in Figure 6, due to the fact that the silicon atom is in solid solution in the iron atom group, making it smaller [32]. At 860K, the lattice constant was the smallest, implying that the distance between atomic layers was the smallest [33]. No nanocrystalline phase containing aluminum atoms was detected in the experiment, which might be due to the minimal quantity of aluminum used. The average grain size of the α-Fe (Si) phase in the core cubic structure of the synthesized Fe based nanocrystalline alloy increased linearly with increasing annealing temperature [34], slowed after 820K, and ultimately tended to roughly 17nm. Simultaneously, the same change trend was reflected in the crystallization fraction change process. The crystallization fraction of the alloy was close to 60% when it reached 820 K or higher. The development of the nanocrystalline alloy was mostly regulated by the crystallization process of the nanocrystalline alloy, according to the aforementioned experimental results. In a summary, the shift in grain size was critical to understanding the nanocrystalline process.

3.4. Magnetic Property Analysis

The magnetic characteristics of the produced Fe based nanocrystalline alloy were tested using a vibration sample magnetometer and a hysteresis loop analyzer, as shown in Figures 7 to 9. Figure 7 shows the relationship between the amplitude permeability and the magnetic field strength of the hysteresis loop analyzer at the frequency of 50 Hz.

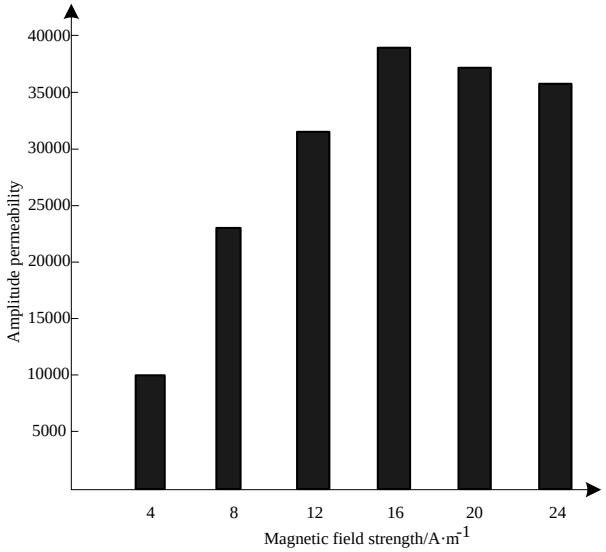

Figure 7. Relationship between amplitude magnetic permeability and magnetic field strength ofFe based nanocrystalline alloy.

The amplitude permeability was around 10,000 when the magnetic field strength was 4 A•m^{-1}, while the maximum permeability was around 39,000 when the magnetic field strength was 16 A•m^{-1}, according to the experimental results in Figure 7. For the Fe based nanocrystalline alloy with high initial permeability, the change rate of amplitude permeability was 280 percent in the relatively large range of 0-12.5 A•m^{-1}, while the change rate of amplitude permeability was 300% to 400% in the field of 0-1.2 A•m^{-1}. Simultaneously, the initial permeability was 23,000, and the saturated magnetic induction strength of the alloy determined by the vibrating sample magnetometer was 1.67 T when the magnetic field intensity was 0.4 A•m^{-1}. Figure 8 shows the relationship between coercive force and annealing temperature of Fe based nanocrystalline alloy prepared by hysteresis loop analyzer at 50 Hz.

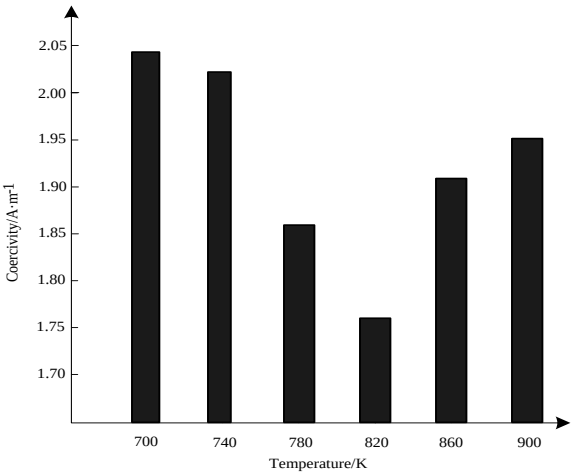

Figure 8. Relationship between coercivity and annealing temperature of Fe based nanocrystalline alloy.

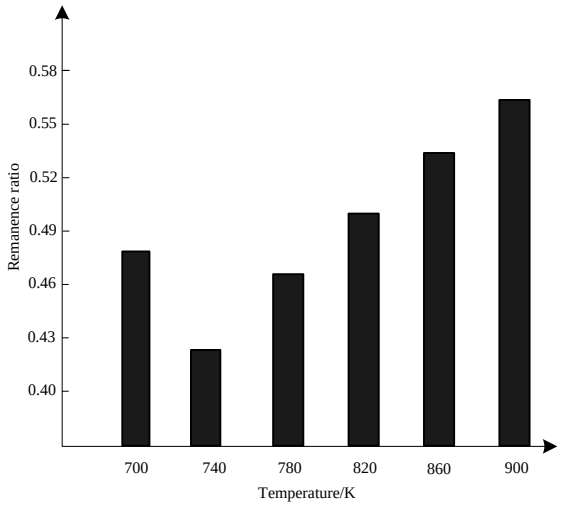

Figure 9. Relationship between remanence ratio and annealing temperature of Fe based nanocrystalline alloy.

The relationship between coercive force and annealing temperature in Figure 8 shows that the minimum coercive force was 1.76 A•m^{-1} when the annealing temperature was 820 K, and then rapidly increases. The coercive force increases to 1.95 A•m^{-1} when the annealing temperature is 900 K. Figure 9 shows the relationship between remanence ratio and annealing temperature of Fe based nanocrystalline alloy prepared by a hysteresis loop analyzer at 50 Hz. As shown in Figure 9, when the annealing temperature was 780 K, the remanence ratio had a significant increase, and when the annealing temperature was 900 K, the remanence ratio reached the maximum value of 0.57 A•m^{-1}.

3.5. Mechanical Property Analysis

In order to characterize the mechanical properties of the prepared nanocrystalline alloy and further study the sensitivity of the iron-based nanocrystalline alloy, the microhardness and elastic

modulus of the prepared iron-based nanocrystalline alloy were measured by the nano indentation method, and the mechanical properties of the iron-based nanocrystalline alloy were compared with those of the coarse-grained alloy. The experimental results are shown in Figure 10 and 11.

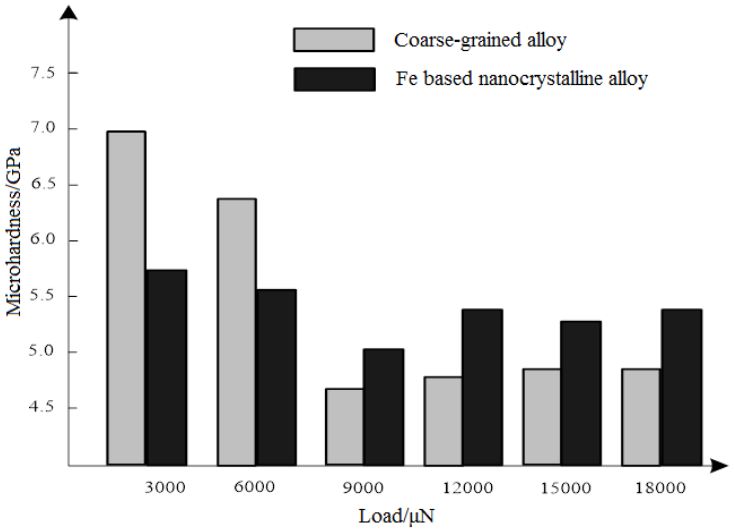

Figure 10. Comparison of micro hardness of different materials

According to the comparison results of microhardness in Figure 10, when the stress was 18,000 μN, the microhardness of the alloy with coarse-grained structure was 4.73 GPa, while that of the iron-based nanocrystalline alloy prepared in this paper was 5.46 GPa. The experimental results show that the microhardness of the iron-based nanocrystalline alloy prepared in this paper was higher than that of the coarse-grained alloy.

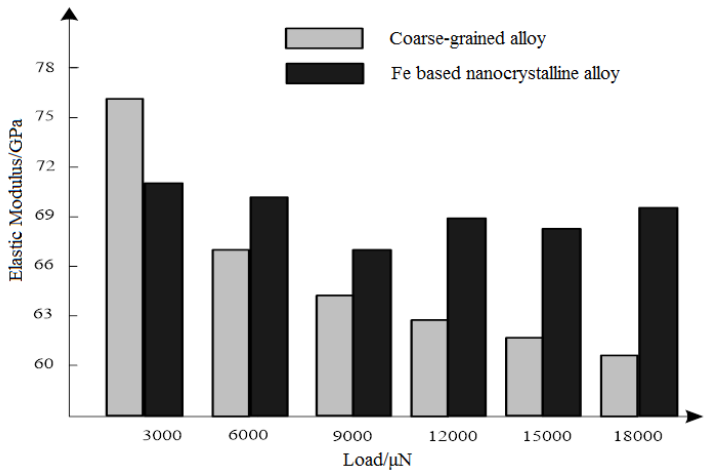

Figure 11. Comparison of elastic modulus of different materials

The elastic modulus of the Fe based nanocrystalline alloy developed in this research was 70.1 GPa when the stress was 18,000 N, whereas that of the coarse-grained alloy was only 60.3 GPa, as shown in the microhardness comparison results in Figure 11. The experimental results reveal that the

Fe-based nanocrystalline alloy developed in this work has a greater elastic modulus than the coarse-grained alloy, which is consistent with previous studies [35, 36]. The main reason for the high microhardness and elastic modulus of the Fe based nanocrystalline alloy is that the dislocation movement in the nanocrystalline alloy is restrained and no longer dominates the deformation process [28, 37]. The deformation was controlled by the grain boundary behavior. Therefore, the microhardness and elastic modulus of the nanocrystalline alloy were higher than those of the coarse-grained alloy.

4. DISCUSSION

Nanocrystalline alloys are a novel type of material that is increasingly being employed in power systems. The solidification sensitivity of Fe-based nanocrystalline alloys was the focus of this work. The use of nanocrystalline alloy materials in power systems offered the following benefits over typical magnetic materials such as silicon steel [38, 39]:

4.1. High Saturation Magnetization

There was no crystal anisotropy in the nanocrystalline alloy material because of the disordered arrangement of atoms, thus the nanocrystalline alloy core had high permeability [40], which gave the nanocrystalline alloy sensor strong magnetism. The saturation magnetic induction strength of Fe-based nanocrystalline alloys was particularly strong, ranging from 1.4 to 1.7 T.

4.2. Low Energy Consumption

Nanocrystalline alloy had a very low core loss, which was 1/3 to 1/5 of that of ordinary silicon steel sheet core, due to its high resistivity [41]. The core loss may be reduced by 60-70% by using nanocrystalline alloy instead of silicon steel as a distribution transformer.

4.3. Simple Production Process and Environmental Protection

Smelting, casting, hot rolling, cold rolling, processing, and annealing are some of the processes used in the manufacturing of traditional crystalline soft magnetic alloys (such as silicon steel) [42, 43]. In comparison to traditional soft magnetic alloys, prepared nanocrystalline alloys offered the advantages of a quick, simple, and energy-efficient procedure.

4.4. Low Price

Due to the simple process, the cost of nano crystalline alloy core is low, which is close to silicon steel sheet, but far lower than permalloy, and has high cost performance.

4.5. High Temperature Stability

When the temperature of commonly used magnetic materials is higher than a certain value, the original magnetic properties of materials will be lost [44]. This temperature is called Curie temperature (or Curie point) [45]. The Curie temperature of nanocrystalline alloy material was higher than 400ºC, and it was stable at high frequency, which ensures a wide range of application. In addition, due to the crystallization of nanocrystalline alloy materials at high temperature, its use temperature was limited by the crystallization temperature. The crystallization temperature of nanocrystalline materials was generally between 450 - 600ºC, which can adapt to the application environment temperature of transformer. As a result, the temperature stability of the nanocrystalline transformer was greater than previously reported [46, 47].

.

4.6. High Aging Stability

Due to the metastable state of nanocrystalline alloy materials, there is a crystallization trend under certain temperature conditions, which leads to the decrease of magnetic properties of nanocrystalline alloy materials with time, but the decrease of this trend temperature shows an exponential law [48]. The nanocrystalline transformer used in the United States has been in normal operation since 1980s [49], and there is no case of aging of transformer due to deterioration of core performance in China. Applications and tests in China and abroad have proved that the use of nanocrystalline alloy materials at 130℃ was reliable, and the use temperature of some varieties can even reach 150℃, which fully shows that nanocrystalline alloy materials were very safe in aging stability.

4.7. Good Magnetic Shock Stability

During the use of a nanocrystalline alloy core, sometimes it will be impacted by strong magnetic field from the inside or outside of the power supply [50]. After the impact of strong magnetic field, it is very important to keep the original performance of the iron core. The deterioration of the core performance will reduce the power efficiency, even cause the core work point deviation, saturate the core and damage the switch tube. The test results show that the magnetic properties of the Fe based nanocrystalline alloy can be basically restored by the impact of a strong magnetic field after proper treatment.

4.8. High Mechanical Stability

Before being used, nanocrystalline alloys are usually heat treated. The material becomes brittle after heat treatment [51]. Most of them must be stored in a protective box or utilized after surface injection when utilized as nanocrystalline cores. When the iron core is placed inside the protective box, some cushions, such as silicone grease and sponge, are normally added [52]. Our findings reveal that the iron core was not damaged throughout usage, and that the magnetic property did not deteriorate, and that the iron core was mechanically stable.

4.9. Wide Frequency Range

Various nanocrystalline alloys have different saturation flux densities and Curie points, making them suitable for both high and low frequency power system operation [53]. The selection of an appropriate nanocrystalline transformer may be used in both high and low frequency power systems.

5. CONCLUSIONS

Nanocrystalline alloy is a new type of soft magnetic material developed in the late 1980s. It has the characteristics of high saturation magnetic induction, high permeability and low high frequency loss. It is an alternative product of traditional soft magnetic materials such as silicon steel, ferrite and permalloy. The amorphous method was used to prepare Fe based nanocrystalline alloy, and the solidification morphology, magnetic properties and mechanical properties of the Fe based nanocrystalline alloy were studied. The results showed that the hardness and elastic modulus of the prepared Fe based nanocrystalline alloy were higher than those of the coarse-grained alloy, and the magnetic properties of the Fe based nanocrystalline alloy prepared at different annealing temperatures were different. According to EIS studies, an undercooling temperature of 360K increases the penetration of electrolyte ions into electrode structures due to the formation of a high surface area and a high electron-transfer rate. Due to the high sensitivity of nanocrystalline alloy, nanocrystalline alloy materials with different magnetic properties are prepared according to the actual demand in the application of power system.

References

1. C. Wan, M. Pan, Q. Zhang, F. Wu, L. Pan and X. Sun, *Sensors and Actuators A: Physical*, 278 (2018) 11.
2. C. Zhou, H. Xu, H. Liu and C. Li, *Journal of Power Supply*, 15 (2017) 125.
3. A.K. Chaudhari and V. Singh, *Journal of Alloys and Compounds*, 751 (2018) 194.
4. H. Karimi-Maleh, Y. Orooji, F. Karimi, M. Alizadeh, M. Baghayeri, J. Rouhi, S. Tajik, H. Beitollahi, S. Agarwal and V.K. Gupta, *Biosensors and Bioelectronics*, 184 (2021) 113252.
5. Y.Y. Leow, C.A. Ooi and M.N. Hamidi, *Electrical Engineering*, 56 (2019) 1.
6. P. Singh, T. Sethi, B.B. Biswal and S.K. Pattanayak, *International Journal of Materials, Mechanics and Manufacturing*, 3 (2015) 249.
7. M. Zhou, D. Zang, X. Zhai, Z. Gao, W. Zhang and C. Wang, *Ceramics International*, 42 (2016) 10704.
8. L. Ding, Z. Wang, X. Wang and D. Wu, *Computer Communications*, 155 (2020) 32.
9. J. Chen, M.A. Tschopp and A.M. Dongare, *Journal of Applied Physics*, 122 (2017) 225901.
10. H. Karimi-Maleh, M.L. Yola, N. Atar, Y. Orooji, F. Karimi, P.S. Kumar, J. Rouhi and M. Baghayeri, *Journal of colloid and interface science*, 592 (2021) 174.
11. I.M. Diahovchenko and R.G. Olsen, *Electric Power Systems Research*, 186 (2020) 106400.
12. J. Guo, G. Haberfehlner, J. Rosalie, L. Li, M.J. Duarte, G. Kothleitner, G. Dehm, Y. He, R. Pippan and Z. Zhang, *Nature communications*, 9 (2018) 1.
13. G. Zimmermann, L. Sturz, H. Nguyen-Thi, N. Mangelinck-Noël, Y. Li, C.-A. Gandin, R. Fleurisson, G. Guillemot, S. Mcfadden and R.P. Mooney, *Jom*, 69 (2017) 1269.

14. D.M. Herlach, S. Burggraf, P. Galenko, C.-A. Gandin, A. Garcia-Escorial, H. Henein, C. Karrasch, A. Mullis, M. Rettenmayr and J. Valloton, *Jom*, 69 (2017) 1303.
15. M. Abdelaziz, E. Elgallad, H. Doty, S. Valtierra and F. Samuel, *Philosophical Magazine*, 99 (2019) 1633.
16. M. Fleck, F. Querfurth and U. Glatzel, *Journal of Materials Research*, 32 (2017) 4605.
17. P. Tippo, P. Singjai, S. Choopun and S. Sakulsermsuk, *Materials Letters*, 211 (2018) 51.
18. D.M. Matson, X. Xiao, J.E. Rodriguez, J. Lee, R.W. Hyers, O. Shuleshova, I. Kaban, S. Schneider, C. Karrasch and S. Burggraff, *Jom*, 69 (2017) 1311.
19. H. Wang, M.S. Hamed and S. Shankar, *Journal of Materials Science*, 53 (2018) 9771.
20. L. Zou, J. Wu, Z. Han, T. Zhao and L. Zhang, *IEEE Transactions on Magnetics*, 54 (2018) 1.
21. B.L. Silva, V.C.E. da Silva, A. Garcia and J.E. Spinelli, *Journal of electronic materials*, 46 (2017) 1754.
22. B. Bergk, U. Mühle and B. Kieback, *Journal of Materials Science*, 53 (2018) 13424.
23. P. Patel, *MRS Bulletin*, 42 (2017) 872.
24. A. Bigos, E. Beltowska-Lehman and M. Kot, *Surface and Coatings Technology*, 317 (2017) 103.
25. C.M. Caneda, J.B. Fogagnolo, C.S. Kiminami and C.R. Afonso, *Materials characterization*, 160 (2020) 110080.
26. T. Nagase, A. Yokoyama and Y. Umakoshi, *Journal of Alloys and Compounds*, 494 (2010) 295.
27. F. Li, T. Liu, J. Zhang, S. Shuang, Q. Wang, A. Wang, J. Wang and Y. Yang, *Materials Today Advances*, 4 (2019) 100027.
28. A. Kumar, R. Kumar, P. Bijalwan, M. Dutta, A. Banerjee and T. Laha, *Journal of Alloys and Compounds*, 771 (2019) 827.
29. C. Bolfarini and V.C. Srivastava, *Metal Sprays and Spray Deposition*, 19 (2017) 521.
30. Y.-L. Shi, M.-F. Shen, S.-D. Xu, X.-Y. Qiu, L. Jiang, Y.-H. Qiang, Q.-C. Zhuang and S.-G. Sun, *Int. J. Electrochem. Sci*, 6 (2011) 3399.
31. J. Zhao, L. Wang, X. He, C. Wan and C. Jiang, *Int. J. Electrochem. Sci*, 5 (2010) 478.
32. P. Ahvenainen, I. Kontro and K. Svedström, *Cellulose*, 23 (2016) 1073.
33. R. Zhang, L. Li, L. Frazer, K.B. Chang, K.R. Poeppelmeier, M.K. Chan and J.R. Guest, *Physical Chemistry Chemical Physics*, 20 (2018) 27456.
34. T. Liu, F. Li, A. Wang, L. Xie, Q. He, J. Luan, A. He, X. Wang, C. Liu and Y. Yang, *Journal of Alloys and Compounds*, 776 (2019) 606.
35. Y.-K. Kim, G.-S. Ham, H.S. Kim and K.-A. Lee, *Intermetallics*, 111 (2019) 106486.
36. D.-H. Lee, M.-Y. Seok, Y. Zhao, I.-C. Choi, J. He, Z. Lu, J.-Y. Suh, U. Ramamurty, M. Kawasaki and T.G. Langdon, *Acta Materialia*, 109 (2016) 314.
37. W. Huo, X. Liu, S. Tan, F. Fang, Z. Xie, J. Shang and J. Jiang, *Applied Surface Science*, 439 (2018) 222.
38. P. Huang, C. Mao, D. Wang, L. Wang, Y. Duan, J. Qiu, G. Xu and H. Cai, *IEEE Transactions on Industrial Electronics*, 64 (2017) 4391.
39. J.-S. Lai and M.W. Ellis, *Proceedings of the IEEE*, 105 (2017) 2166.
40. J. Liang, F. Ma, S. Hwang, X. Wang, J. Sokolowski, Q. Li, G. Wu and D. Su, *Joule*, 3 (2019) 956.
41. A. Najafi and I. Iskender, *Electrical Engineering*, 100 (2018) 1125.
42. R. Parsons, B. Zang, K. Onodera, H. Kishimoto, T. Shoji, A. Kato and K. Suzuki, *Journal of Magnetism and Magnetic Materials*, 476 (2019) 142.
43. A. Makino, *IEEE Transactions on Magnetics*, 48 (2012) 1331.
44. R. Wildeboer, P. Southern and Q. Pankhurst, *Journal of Physics D: Applied Physics*, 47 (2014) 495003.

45. M. Kurniawan, A. Perrin, P. Xu, V. Keylin and M. McHenry, *IEEE Magnetics Letters*, 7 (2016) 1.
46. A.K. Paul, *IEEE Transactions on Industry Applications*, 56 (2020) 970.
47. P. Jusner, E. Schwaiger, A. Potthast and T. Rosenau, *Carbohydrate Polymers*, 25 (2020) 117196.
48. T. Gheiratmand and H.M. Hosseini, *Journal of Magnetism and Magnetic Materials*, 408 (2016) 177.
49. A.L. Greer, *Science*, 267 (1995) 1947.
50. H.T. Le, Y. Nour, Z. Pavlovic, C. O'Mathúna, A. Knott, F. Jensen, A. Han, S. Kulkarni and Z. Ouyang, *IEEE Transactions on Power Electronics*, 34 (2018) 74.
51. A. Detor and C. Schuh, *Journal of Materials Research*, 22 (2007) 3233.
52. L. Hou, W. Yang, Q. Luo, X. Fan, H. Liu and B. Shen, *Journal of Non-Crystalline Solids*, 530 (2020) 119800.
53. L. Shi and K. Yao, *Materials & Design*, 189 (2020) 108511.

© 2021 The Authors. Published by ESG (www.electrochemsci.org). This article is an open access article distributed under the terms and conditions of the Creative Commons Attribution license (http://creativecommons.org/licenses/by/4.0/).